Effect of electron-electron scattering on nonequilibrium transport in quantum-well systems

S. M. Goodnick
Department of Electrical and Computer Engineering, Oregon State University, Corvallis, Oregon 97331

P. Lugli
Dipartimento di Fisica, Università di Modena, 41100 Modena, Italy
(Received 22 June 1987)

We model nonequilibrium transport in a GaAs-$Al_xGa_{1-x}As$ quantum-well structure using an ensemble Monte Carlo simulation of the full multisubband system in which we include electron-electron (*e-e*) scattering explicitly into the calculation. The *e-e* scattering cross section is calculated using the Born approximation and introduced into the transient Monte Carlo simulation via a self-scattering technique. This interaction is found to be especially effective in transferring energy between different subbands, thus thermalizing the carriers within a picosecond. The model described herein is applied to the study of laser-excited carriers in a quantum-well system and to the response of such a system to high parallel electric fields. In the case of laser excitation, *e-e* interaction may dominate the initial evolution, reducing the cascade of carriers via optical-phonon emission.

I. INTRODUCTION

Recent time-resolved bleaching studies of the initial relaxation of photoinjected carriers in bulk GaAs (Ref. 1) and GaAs-$Al_xGa_{1-x}As$ (Ref. 2) quantum wells (QW) have shown the apparent evolution of the electron distribution as a function of time on the subpicosecond time scale. On this time scale, the electron (and hole) distribution functions evolve from a highly nonequilibrium Gaussian pulse centered around the excitation energy in the band to a heated Maxwellian (thermalized) distribution on the order of a few tenths of a picosecond. This time scale is short enough that polar-optical-phonon (POP) scattering has not relaxed a significant portion of the energy, and thus the distribution is thermalized through intercarrier interaction. Time-resolved photoluminescence measurements have also been reported which show that the distribution function on the picosecond time scale is thermalized and Fermi-like.[3-5] However, under certain conditions, cw luminescence experiments show a cascadelike distribution arising from successive phonon emission of electrons as they cool.[6] In these experiments carrier-carrier scattering is less dominant and a nonthermal distribution is maintained.

In the present work we model the picosecond time-scale dynamical behavior of electrons confined in a quantum well using an ensemble Monte Carlo simulation which includes *e-e* scattering, degeneracy, and the inclusion of nonequilibrium phonons. We previously used this model to simulate the dynamics of photoexcited carriers in a QW system, the results of which showed that carrier cooling in such systems is controlled by hot-phonon buildup.[7,8] Here we present details of the model used in the previous work and apply it to the study of the subpicosecond response in quantum-well systems to both optical and electrical excitation. In the present paper we will concentrate on the model for *e-e* scattering in a QW system and reserve discussion of hot phonons for future work. In the next section (II), details of the Monte Carlo transport simulation for a model QW system are given. The following section (III) will show the results of this simulation for the steady-state distribution function of electrons subject to an applied electric field. Results will then be presented for the carrier evolution under laser excitation in the presence of *e-e* scattering assuming temperature-independent screening. This evolution, which depends substantially on the electron density, is found to evolve as a cascade of phonon emission only for very low injected densities (10^{10} cm^{-2}). For higher densities, *e-e* scattering broadens the injected carrier energy sufficiently fast to wash out peaks in the distribution arising from phonon emission. Due to the high rate of intersubband energy exchange, a common energy is achieved between the different subbands shortly after the end of the laser pulse.

II. MODEL

In the present section we describe the model used in calculating the nonequilibrium response of a quantum-well system using an ensemble Monte Carlo simulation. Results of Monte Carlo simulation on transport in quasi-two-dimensional systems have been reported previously by other authors.[9-11] In our model for the quantum-well system, all scattering rates are calculated from their two-dimensional forms including both intra- and intersubband scattering processes. We have included the effects of polar-optical-phonon scattering (bulk modes), intervalley scattering with the satellite *L* valleys, also assumed quantized, impurity scattering (from a

sheet of impurities[12]), and finally electron-electron scattering. Degeneracy of the final state is also accounted for in our simulation so that low-temperature transport may be modeled. Typically, in the ensemble Monte Carlo we model the motion of 2000–5000 electrons whose free flight times and scattering events are generated stochastically from the various probabilities for scattering and the random-number generator on the computer. From this we tabulate the instantaneous distribution function of the electrons (and phonons when nonequilibrium effects are included) from which various macroscopic quantities may be calculated. In the following, we detail the model employed in the description of the quantum-well system and of the various scattering mechanisms. We also discuss the algorithm used to incorporate multisubband *e-e* scattering and degeneracy effects into the Monte Carlo simulation.

A. Quantum-well system

As a model quasi-two-dimensional system, we consider a finite square-well potential defined by the conduction-band offset between undoped GaAs and $Al_{0.23}Ga_{0.77}As$ which we take as 0.28 eV. The subband energies and eigenfunctions in the central valley are calculated from the solution of the one-dimensional effective-mass equation for this potential. The envelope functions then satisfy the separable form[13]

$$\Psi(R)=\zeta_i(z)e^{i\mathbf{k}\cdot\mathbf{r}}/A \ , \tag{2.1}$$

where R is the position vector, r and k are the position and wave vectors in the plane parallel to the well, z is the normal direction, and A is the normalization area. The scattering rates discussed below are calculated fully numerically, and thus we are not limited to a simple square well employed here for simplicity. Results using a full self-consistent calculation including exchange and correlation effects have been discussed elsewhere.[12] We consider the L valley as quantized although the barrier height in the upper valleys is not well known and is expected to be less than that of the central valley. Here we assume the same barrier in the L valley as the central valley (0.28 eV) and assume solutions in the form of (2.1).

B. Polar optical scattering

Longitudinal polar-optical-phonon scattering is a dominant energy-loss mechanism in GaAs, at least at high carrier temperatures. In the quantum well we assume that the two-dimensional (2D) electrons interact with bulk phonon modes via the Fröhlich interaction.[14,15] Quantization of the phonon modes (or slab modes) has been considered to some extent by Riddoch and Ridley,[16] who found significant deviations in the scattering rates for well widths less than about 100 Å. The effect of screening of the longitudinal-optical (LO) interaction is not clear, especially in 2D. Static screening leads to gross overestimation of this interaction, and thus a full dynamical calculation is required.[17,18] If one assumes only bulk screening of longitudinal modes, then the matrix element for scattering is given by[14]

$$|\langle \mathbf{k}\pm\mathbf{q},j\,|\,H\,|\,\mathbf{k},i\rangle|^2=\frac{2\pi\hbar^2eE_0(q^2+q_z^2)}{Vm^*(q^2+q_z^2+q_s^2)^2}\times(n_{\omega_0}+\tfrac{1}{2}\mp\tfrac{1}{2})\,|\,G_{ij}(q_z)\,|^2 \ , \tag{2.2}$$

where q and q_z are the parallel and normal components of the phonon wave vector, q_s is the 3D inverse screening length, m^* is the effective mass, i and j denote the initial and final subband indices, and the effective field eE_0 is given by

$$eE_0=\frac{m^*e^2\hbar\omega_0}{\hbar^2}\left[\frac{1}{\kappa_\infty}-\frac{1}{\kappa_0}\right] \tag{2.3}$$

with κ_0 and κ_∞ the low- and high-energy dielectric constants, and $\hbar\omega_0$ is the phonon energy. The overlap integral $|\,G_{ij}(q_z)\,|^2$ is given by

$$|\,G_{ij}(q_z)\,|^2=\int_{-\infty}^{\infty}dz\int_{-\infty}^{\infty}dz'\rho_{ij}(z)\rho_{ij}^*(z')e^{iq_z(z-z')} \ , \tag{2.4a}$$

$$\rho_{ij}(z)=\zeta_i^*(z)\zeta_j(z) \ , \tag{2.4b}$$

between initial and final subbands. This function, which is related to the momentum uncertainty due to the spatial confinement of the electrons, is peaked for q_z corresponding to the parabolic momentum associated with the initial- and final-state subband energies. By converting the sum over q_z to an integral, the q_z dependence may be integrated analytically to yield a smooth function which is better suited for numerical evaluation of the scattering rate. Thus we define the function

$$I(q,z,z')=\int_{-\infty}^{\infty}dq_z\frac{(q^2+q_z^2)}{(q^2+q_z^2+q_s^2)^2}e^{iq_z(z-z')} \ , \tag{2.5}$$

which may be evaluated by contour integration to yield

$$I(q,z,z')=\frac{\exp[-(q^2+q_s^2)^{1/2}\,|\,z-z'\,|\,]}{(q^2+q_s^2)^{1/2}}\times\left[1-\frac{|\,z-z'\,|\,q_s^2}{2(q^2+q_s^2)^{1/2}}-\frac{q_s^2}{2(q^2+q_s^2)}\right] \ , \tag{2.6}$$

which in the unscreened case ($q_0=0$) gives the same result as Price.[19] The total scattering rate may thus be written

$$\Gamma_{ij}(k)=\frac{eE_0}{2\hbar}\left[n_{\omega_0}\int_0^{2\pi}\frac{H_{ij}(q_+)}{(q_+^2+q_s^2)^{1/2}}+(n_{\omega_0}+1)\int_0^{2\pi}d\theta\frac{H_{ij}(q_-)}{(q_-^2+q_s^2)^{1/2}}\right] \ , \tag{2.7}$$

where the function H_{ij} is defined from the integration over the envelope functions

$$\frac{H_{ij}(q)}{(q^2+q_s^2)^{1/2}}=\int_{-\infty}^{\infty}dz\int_{-\infty}^{\infty}dz'\rho_{ij}(z)\rho_{ij}^*(z')I(q,z,z') \tag{2.8}$$

with $I(q,z,z')$ given in (2.6). The + and − signs on q in (2.7) refer to absorption and emission, respectively, for the scattered wave vector given by

$$q=|\mathbf{k}-\mathbf{k}'|=\left[2k^2\pm\frac{2\omega_{ij}^* m^*}{\hbar}-2k\left[k^2\pm\frac{2\omega_{ij}^* m^*}{\hbar}\right]^{1/2}\cos\theta\right]^{1/2}, \tag{2.9a}$$

$$\hbar\omega_{ij}^*=\hbar\omega_0\pm(E_i-E_j)\,, \tag{2.9b}$$

where $\hbar\omega_{ij}^*$ serves as an effective phonon energy which depends on the initial and final subband energies E_i and E_j. The scattering rate (2.7) is shown for a 150-Å well in Fig. 1 where $i=1$ and we sum over j (total scattering rate from the bottom subband). For comparison we plot the 3D rate as well. We take $q_s=0$ for this calculation. As seen in Fig. 1, the 2D rate is a piecewise approximation of the 3D rate due to the discontinuities in the 2D density of states at the various subband energies.

If nonequilibrium phonons are considered, the phonon occupation factors are no longer independent of q and q_z and thus cannot be taken as constant. In the Monte Carlo simulation we can account for this dependence through the use of self-scattering. Here, n_{ω_0} is replaced by its maximum value during the simulation (which must be set *a priori*), and after every scattering event a rejection technique is used to compare the maximum scattering rate to its actual value determined by the instantaneous value of the phonon distribution.

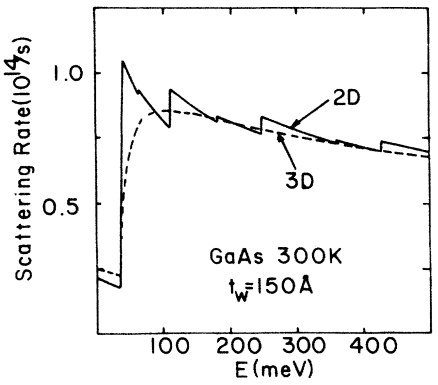

FIG. 1. Total scattering rate due to POP scattering for a 150-Å well for electrons in the first subband (solid line). The dashed line is the 3D scattering rate.

C. Intervalley scattering

Intervalley scattering for two-dimensional systems has been treated previously in connection with Si inversion layers.[20] In the GaAs-$Al_xGa_{1-x}As$ system, it is not clear to what degree quantization plays a role in the upper L and X valleys of the GaAs as the band offset is expected to be smaller there. For simplicity, we consider only quantized upper L valley states in the GaAs with the same barrier as the central valley. For zeroth-order interaction, the matrix element for scattering is given by

$$|H_{\mathbf{k}\mathbf{k}'}^{ij}|_{\rm iv}^2=\frac{\hbar E_{\rm iv}^2(n_{\omega_{\rm iv}}+\frac{1}{2}\mp\frac{1}{2})I_{\rm iv}}{2\rho A\omega_{\rm iv}}\,, \tag{2.10}$$

where $E_{\rm iv}$ is the intervalley deformation potential, ρ is the mass density, and $\omega_{\rm iv}$ is the intervalley phonon frequency. $I_{\rm iv}$ is an overlap integral given by

$$I_{\rm iv}=\int_{-\infty}^{\infty}dz\,|\zeta_i^{v_i}(z)|^2\,|\zeta_j^{v_f}(z)|^2\,, \tag{2.11}$$

where v_i and v_f refer to the initial and final valley envelope functions. The total scattering rate is thus given by

$$\Gamma_{ij}(k)=\sum_{v_f}m_f^*\frac{E_{\rm iv}^2(n_{\omega_{\rm iv}}+\frac{1}{2}\mp\frac{1}{2})I_{\rm iv}}{2\rho\omega_{\rm iv}\hbar^2} \tag{2.12}$$

with m_f^* being the effective mass in the final-state valley and the sum is over all the final-state valleys. We consider a GaAs(100) layer and thus the subbands of the four satellite L valleys are degenerate.

D. Electron-electron scattering

The e-e scattering rate in bulk materials has been previously calculated using the Born approximation.[21–24] This method has been criticized as overestimating the scattering rate by as much as 5 times in sodium[22] compared to computation based on the more-accurate phase-shift method, although the degree of this error in semiconductors is not known. As a first approach to this problem in a quantum-well system, we will adopt the Born approximation in our calculation.

We start by considering the scattering rate between an electron in the well with wave vector $\mathbf{k}$ in subband i and a second electron with wave vector $\mathbf{k}_0$ in subband j. The final states of these two electrons are $\mathbf{k}'$ and m for the first electron and $\mathbf{k}_0'$ and n for the second electron. The unscreened matrix element between these two initial and final states may be written

$$H_{\substack{\mathbf{k},\mathbf{k}'\mathbf{k}_0,\mathbf{k}_0'\\ i,m,j,n}}^{ee}=\frac{e^2}{\kappa}\int_{-\infty}^{\infty}dz\int_{-\infty}^{\infty}dz'\int d\mathbf{r}\int d\mathbf{r}'\frac{e^{-i(\mathbf{k}\cdot\mathbf{r}+\mathbf{k}_0\cdot\mathbf{r}')}e^{i(\mathbf{k}\cdot\mathbf{r}+\mathbf{k}\cdot\mathbf{r}_0')}}{[|\mathbf{r}-\mathbf{r}'|+(z-z')^2]^{1/2}}\zeta_i(z)\zeta_j(z')\zeta_m^*(z)\zeta_n^*(z')\,. \tag{2.13}$$

Introducing the two-dimensional Fourier transform of the Coulomb potential in (2.13), the matrix element becomes

$$H_{\substack{\mathbf{k},\mathbf{k}',\mathbf{k}_0\mathbf{k}_0'\\ i,m,j,n}}^{ee}=\frac{2\pi e^2\delta(\mathbf{k}'+\mathbf{k}_0'-\mathbf{k}-\mathbf{k}_0)}{A\kappa q}F_{ijmn}(q) \tag{2.14}$$

with $q=|\mathbf{k}-\mathbf{k}'|$ and the form factor given by

$$F_{ijmn}(q)=\int_{-\infty}^{\infty}dz\int_{-\infty}^{\infty}dz'\zeta_i(z)\zeta_j(z')\times\zeta_m^*(z)\zeta_n^*(z')e^{-q|z-z'|}\ . \tag{2.15}$$

This form factor appears in the 2D random-phase-approximation (RPA) dielectric function[13] and is somewhat similar to that appearing in phonon scattering[15] as well. As will be discussed later, this form factor is important in determining the relative magnitude of the *e-e* scattering and favors intrasubband over intersubband transitions. Screening in the multisubband 2D system is quantitatively difficult, requiring an inversion of the dielectric matrix in the RPA.[25] For single-subband static screening, the RPA dielectric function in the long-wavelength limit is characterized by a single wave-vector-independent constant (the inverse screening length) which is independent of carrier density at low temperature[26] and proportional to density under nondegenerate conditions.[27] The square of the matrix element is thus given by

$$|H^{ee}|^2=\frac{4\pi^2e^4\delta(\mathbf{k}'+\mathbf{k}_0'-\mathbf{k}-\mathbf{k}_0)}{A^2\kappa^2(q+q_0)^2}|F_{ijmn}(q)|^2 \tag{2.16}$$

with q_0 the inverse screening length in two dimensions. For simplicity, we assume q_0 is given by the low-temperature limit in the present results. When temperature-dependent and multisubband effects are included in q_0, the *e-e* scattering rate is enhanced due to a decrease in the screening constant. Results in which we consider temperature-dependent and multisubband screening are reported elsewhere.[28] In the Born approximation, the total scattering rate out of the first electron in an initial state $\mathbf{k},i$ to a final state in subband m is then calculated from the sum over the final states

$$\Gamma_{im}(\mathbf{k})=\frac{2\pi e^4}{\hbar\kappa A}\sum_{\mathbf{k}_0,j,n}{}'f_j(\mathbf{k}_0)\int d\mathbf{k}_0'\frac{|F_{ijmn}(q)|^2}{(q+q_0)^2}\times\delta(E_i-E_f)\ , \tag{2.17}$$

where use has been made of the δ function in (2.16) to eliminate the sum over $\mathbf{k}'=\mathbf{k}+\mathbf{k}_0-\mathbf{k}_0'$. The δ function in (2.17) represents conservation of energy between the initial and final state and $f_j(\mathbf{k}_0)$ is the carrier distribution function. The prime on the summation indicates that the sum is only over electrons with antiparallel spin. Thus we neglect scattering with carriers at parallel spin which is lower in magnitude than the scattering due to antiparallel electrons due to exchange considerations.[24]

As in the three-dimensional case,[23] it is useful to introduce the relative wave vectors

$$\mathbf{g}=\mathbf{k}_0-\mathbf{k},\quad \mathbf{g}'=\mathbf{k}_0'-\mathbf{k}' \tag{2.18}$$

so that (2.17) may be rewritten

$$\Gamma_{im}(k)=\frac{2\pi e^4}{\hbar\kappa^2 A}\sum_{\mathbf{k}_0,j,n}{}'f_j(\mathbf{k}_0)\int d\mathbf{g}'\frac{|F_{ijmn}(|\mathbf{g}-\mathbf{g}'|/2)|^2}{(|\mathbf{g}-\mathbf{g}'|/2+q_0)^2}\times\delta(E_i-E_f)\ , \tag{2.19}$$

and the argument of the δ function between initial- and final-state energies is

$$\delta(E_i-E_f)=\delta\left[\frac{\hbar^2g^2}{4m^*}-\frac{\hbar^2g'^2}{4m^*}+E_s\right] \tag{2.20}$$

with $E_s=E_i+E_j-E_m-E_n$. This δ function may be used then to reduce the integral over g' to

$$\Gamma_{im}(k)=\frac{4\pi e^4m^*}{\hbar^3A\kappa^2}\sum_{\mathbf{k}_0,j,n}{}'f_j(\mathbf{k}_0)\int_0^{2\pi}d\theta\frac{|F_{ijmn}(q)|^2}{(q+q_{s0})^2}\ , \tag{2.21}$$

where q is related to θ, the angle between g and g', by

$$q=|\mathbf{g}-\mathbf{g}'|/2=[2g^2+g_0^2-2g(g^2+g_0^2)^{1/2}\cos\theta]^{1/2}/2\ , \tag{2.22}$$

and g_0^2 is $4m^*E_s/\hbar^2$. In the case of intrasubband scattering, $g_0=0$ and q is simply

$$q=g\sin\theta/2\ . \tag{2.23}$$

The total scattering rate (2.21) depends on the square of the form factor (2.15) which plotted in Fig. 2 for the

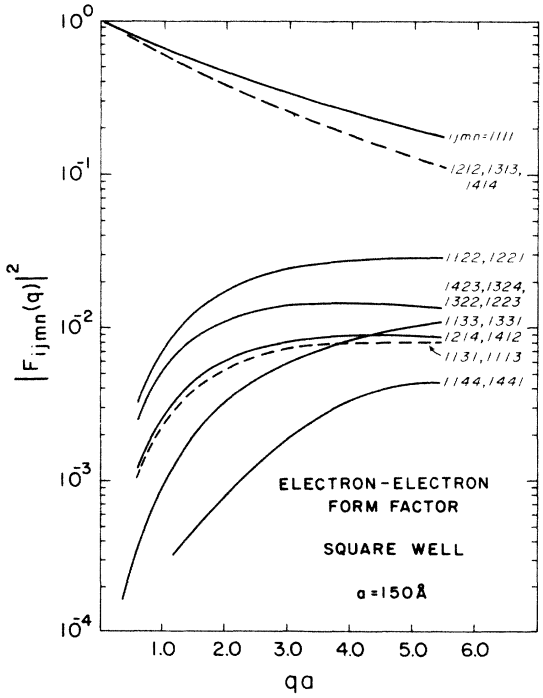

FIG. 2. Electron-electron form factor as a function of wave vector for a 150-Å square well. The indices *ijmn* label initial and final subband states.

dominant terms involving the first electron in the lowest subband. The dominant term occurs for pure intrasubband scattering ($ijmn=1111$) in which the initial and final subband for both electrons is the lowest subband. Of similar value is the form factor for intrasubband scattering in which the initial subbands of the two electrons are different, although they stay within their respective subbands after scattering ($i=m$ and $j=n$). This inelastic scattering between subbands allows energy to be transferred from hot subbands to cold subbands so that a uniform energy is quickly reached between different subbands. Since $g_0=0$ for intrasubband transitions, the scattering rates are peaked for $q=0$ and small-angle scattering is favored.

The intersubband scattering form factor is much lower in magnitude and vanishes for $q=0$ due to the orthagonality of the eigenfunctions in (2.15). Strong interference effects occur in (2.15) so that certain combinations of initial and final subband states result in negligibly small form factors. For the 150-Å well shown in Fig. 2, the dominant intersubband form factors are shown. The transitions 1221, 1331, and 1441 are exchange transitions in which the first and second electrons exchange subbands. Such transitions are similar in effect to intrasubband scattering as the net particle flux from one subband to another is zero. The other transitions do, however, allow a net intersubband particle diffusion. However, as shown in Fig. 2, the form factor is almost 2 orders of magnitude less than the intrasubband value, and thus the mass transfer rate between subbands may be considerably reduced leading to transient bottleneck effects in the subband populations when the 2D system is driven far from equilibrium. The reduction in intersubband scattering is further enhanced due to the nonzero value of g_0 in the denominator, which decreases the scattering rate. However, a similar form factor to (2.15) multiplies the screening constant as well,[13] so that reduced screening could enhance the intersubband rate. More work is needed on the full multisubband screening in order to determine which effect dominates.

E. Monte Carlo simulation

We have included the various scattering mechanisms discussed above into the framework of an ensemble k-space Monte Carlo simulation. Monte Carlo techniques as applied to semiconductor transport have been reviewed by Jacoboni and Reggiani.[29] For the quasi-two-dimensional QW systems, we include both intra- and intersubband scattering in the simulation, both within the same valley and between different valleys. Only two-dimensional transport has been considered in the plane parallel to the well, and thus vertical transport effects over the well (such as real-space transfer) are not included in the simulation. For the results presented here, we neglect any screening of the phonon modes and thus $q_s=0$ in (2.7). Typically, we follow an ensemble of 5000 electrons from which we calculate the electron distribution function, the mean velocity, and mean energy in each subband.

The exclusion principle modifies the scattering rates discussed previously, and this effect must be included in the nonequilibrium behavior at low temperatures and high carrier densities. The inclusion of this effect in a Monte Carlo simulation has been reported by Bosi and co-workers[30] In the multisubband QW system, we account for degeneracy by tabulating the electron distribution function within each subband during the simulation using a self-scattering rejection technique to accept or reject scattering events based on the final-state occupancy.[31] Using this technique (and including e-e scattering discussed below), the equilibrium distribution function in the Monte Carlo simulation attains the proper Fermi-Dirac function of the multisubband system.

The inclusion of hot phonons in the simulation is accomplished through a detailed balance of LO-phonon emission and absorption from which the phonon distribution function is determined. From this distribution function, the electron-phonon scattering rate is subsequently updated through (2.7).[7,8] A variable self-scattering is used to account for the change of this rate during the simulation.

We include e-e scattering into the QW simulation using a modification of the self-scattering technique proposed by Brunetti *et al.*[32] for the bulk. Here we take the full multisubband scattering rate given by (2.21) and maximize the quantity inside of the integral, i.e., choose a maximizing function that is integrable, calculate the total scattering rate based on the new function, and account for the actual value of the function when the final state is chosen through a rejection method. For the intrasubband scattering rate in (2.21), we note that the integrand is sharply peaked at $q=0$ corresponding to $\theta=0$ and 2π. Since the form factor is always unity or less, the maximum value of the integrand is always less than $1/q_0^2$. Thus, the maximum scattering rate is given by

$$\Gamma_{\max,ii}=\frac{4\pi^2 e^4 m^* N_s}{\hbar^3 \kappa^2 q_0^2} , \tag{2.24}$$

where N_s is the total sheet density of the QW and the total rate has been multiplied by $\frac{1}{2}$ due to neglect of parallel spin scattering. This scattering rate is used to generate the free flight time during the simulation. Similarly, for intersubband scattering, the maximum scattering rate from an initial subband i to a final subband m may be written

$$\Gamma_{\max,im}=\Gamma_{\max,ii} F_{\max}^2 N_{\text{sub}} , \tag{2.25}$$

where N_{sub} is the total number of subbands, and $F_{\max}$ is the maximum value of the form factor, (2.15), for intersubband scattering (which is much less than unity as seen in Fig. 2). When e-e scattering is chosen, another electron is chosen at random from the ensemble, and the scattering angle is chosen at random according to the flat distribution associated with the maximizing function. Using another random number between zero and the maximum value of the integrand ($1/q_0^2$), the actual value of the integrand is compared to that of the random number, and the scattering is rejected if the integrand is less than this number. In this case, the electron and its counterpart are then allowed to continue on their origi-

nal flights unchanged. If the random number is less than the integrand value, then the scattering is accepted, the momentum and energy changed accordingly, and a new flight generated. In this technique, considerable computation time is lost via self-scattering events. Depending on the exact electron dynamics, the number of self-scattering events may be 10–100 times the number of real events. However, considerable savings in time is achieved because the scattering rate does not have to be continually recalculated as the electron distribution function changes. Also, the algorithm is quite simple to implement in the context of the usual Monte Carlo program. Degeneracy effects are also included by checking the occupancy of the final states of both electrons and using a rejection technique as discussed earlier.

In general, the total number of particles is not constant (e.g., during optical injection). Also, the screening constant depends strongly on the electron distribution which changes as well, and thus the *e-e* scattering rate changes during the simulation. Therefore, at the beginning of the simulation, the maximum *e-e* scattering rate which will occur during the simulation must be known. During the simulation, the *e-e* rate will vary within this maximum rate. The tabulation of all the scattering rates used to generate the termination of the electron free flights is shown schematically in Fig. 3. When the free flight of the electron is ended, a random number between 0 and Γ is chosen, selecting one of the mechanisms shown in Fig. 3. As shown, self-scattering is divided between *e-e* scattering and the other scattering mechanisms. If *e-e* scattering is chosen to terminate a flight, we first check to see if this is a real event or self-scattering. Then as discussed above, a second possibility for self-scattering arises from the choice of final state and degeneracy. The accuracy of this method is improved as the number of simulated particles is increased and if time steps that are shorter than the collision time are used (the time over which the distribution can change appreciably). We use a time step of 10 fs in the present work which satisfies this requirement. Satisfactory results were obtained with 5000 electrons, and the results were not found to vary with the inclusion of more particles (only the statistical uncertainty is improved). We include *e-e* scattering only for the central valley electrons and neglect this interaction in the *L* valley.

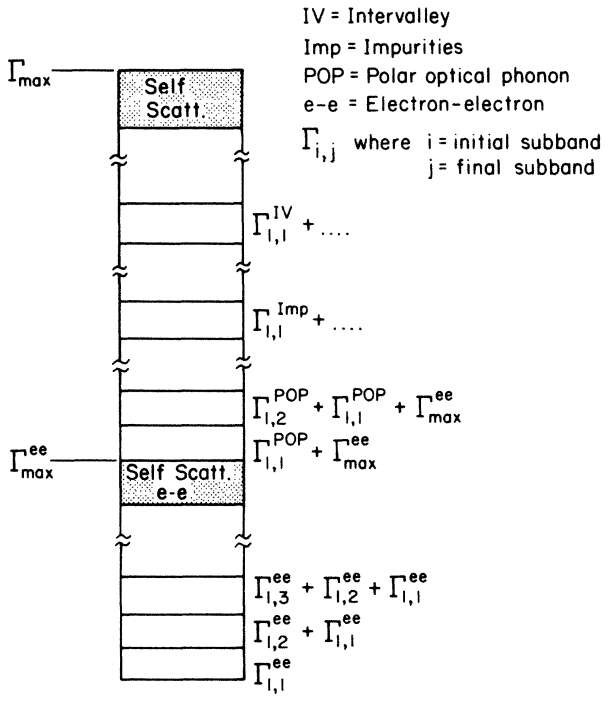

FIG. 3. Histogram of the various scattering rates in the Monte Carlo simulation.

III. RESULTS AND DISCUSSION

A. Hot-carrier behavior in a uniform electric field

Electron-electron scattering exchanges energy between carriers thus redistributing the energy gained by an electric field and driving the electron distribution function towards a Maxwellian-type distribution. In polar semiconductors, the threshold in energy for optical-phonon emission results in a sharp increase in the scattering rate which tends to deplete the population of electrons above the threshold energy. Thus, in the presence of strong polar-optical-phonon scattering, the electron distribution function cuts off at the emission threshold, while *e-e* scattering has the effect of repopulating the high-energy tail. Figure 4 shows the steady-state electron distribution function in the lowest subband with and without *e-e* scattering in a uniform field of 0.5 kV/cm at 20 K. A carrier density of 4×10^{11} cm^{-2} was assumed which is a typical value for GaAs-$Al_xGa_{1-x}As$ quantum wells. Hot phonons were not considered in the results in which electric fields were present. Without *e-e* scattering, the distribution function is well represented by a two-temperature model in which electrons above the threshold are depleted to lower energies via phonon emission. The kink in the distribution function is removed with *e-e* scattering present due to inelastic scattering above the phonon threshold. Such a result has been observed in bulk Monte Carlo simulation of *e-e* interaction as well.[23]

In Fig. 5 we show the electron occupation versus energy for a 258-Å well with four subbands in the well. The energies of the subband levels are shown by the arrows in Fig. 5. The normalized electron density (which is the distribution times the density of states) is shown for three different applied electric fields corresponding to the fields used by Shah *et al.*[33] in studying the carrier heating in similar width quantum wells using photoluminescence (PL). At the first excited subband energy, a kink in the density is observed in Fig. 5 due to the presence of carriers in the second subband, similar to the results of PL studies. We see very little structure in the occupation at the next subband however. In fact, we see a depletion of the higher subbands due to the fact that electron may transfer from a higher subband to a lower one by phonon emission for any energy (unless the subband spacing is less than the phonon energy). However, to make an intersubband scattering to a higher subband via

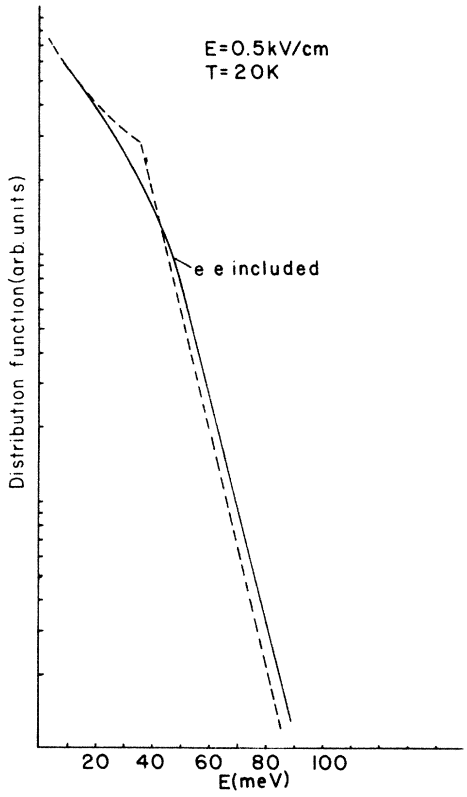

FIG. 4. Steady-state electron distribution function for an applied field of 0.5 kV/cm in a single subband system.

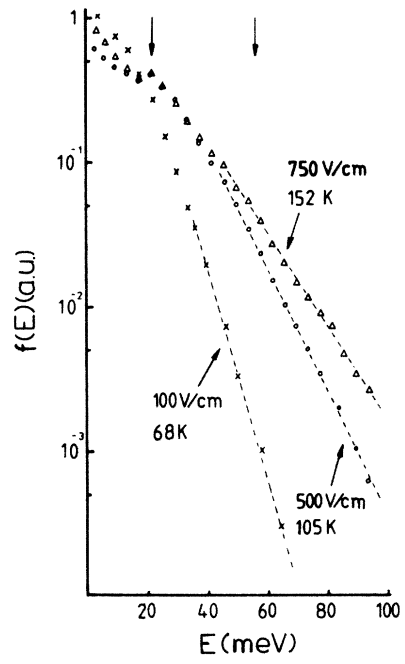

FIG. 5. Steady-state distribution function for a 258-Å well for various applied electric fields. The arrows denote the energies of the first and second excited subbands.

phonon emission requires that the electron be one phonon energy above the subband energy itself. Since at low temperature absorption is negligible, there is a tendency towards depleting the bottoms of the higher subbands. This is still found to be true with *e-e* scattering present in the constant screening approximation as the intersubband *e-e* scattering rate is less than that of POP scattering.

The carrier "temperatures" are found from the high-energy slope as shown in Fig. 5. We find values of 68, 105, and 152 K for electric fields of 100, 500, and 750 V/cm, respectively. Note that these temperatures do not correspond to the average carrier energies due to the effect of degeneracy, the latter values being larger. The electron temperatures measured in PL studies are 100, 145, and 165 K for the same fields[33] which are consistently higher than those calculated here. The reason for this difference is not understood at this time, although screening of the LO interaction or hot phonons could play a role.

In Fig. 6 we show the transient electron drift velocity as a function of time for an electric field of 5 kV/cm applied at time $t=0$ to an electron gas originally at 77 K in equilibrium. The results are shown both with and without *e-e* scattering and the difference is very marginal due to the fact that the total wave vector of both electrons is conserved for *e-e* scattering, and therefore no change in the momentum in the direction of the field is expected. As shown by the dashed line of Fig. 6, electrons are accelerated quasiballistically during the first 0.2 ps even though numerous *e-e* collisions have occurred during this time interval.

B. Photoexcitation into the quantum well

Numerous investigations have been made of the relaxation of hot carriers injected into multiple quantum wells.[34] The initial relaxation dynamics are strongly

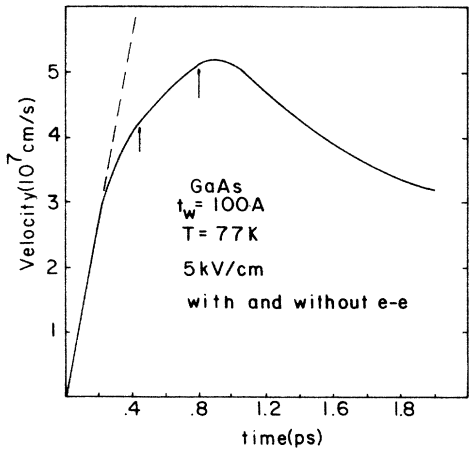

FIG. 6. Velocity vs time after an applied electric field of 5 kV/cm to a 100-Å well (two subbands). The arrows denote the onset of intersubband transfer (first arrow) and intervalley transfer. The dashed curve is the velocity free acceleration of the carriers without collisions.

influenced by *e-e* interaction. If *e-e* scattering is weak, the injected electrons relax in a cascade of subsequent polar-optical-phonon emission. The nonequilibrium distribution would appear as a series of peaks starting at the injection energy and separated by $\hbar\omega_0$ to the bottom of the band. If *e-e* scattering is strong, then the electrons are scattered several times before optical-phonon emission and thus memory of the initial injection energy is eliminated. In this case, electrons cool by phonon emission from a thermalized distribution rather than a cascade.

To study the initial dynamics, we simulate the injection of carriers monoenergetically into the conduction band of the quantum well. To model the time dependence of the carrier injection through femtosecond laser excitation, we add carriers monoenergetically into the Monte Carlo simulation according to the following equation:[35]

$$G(t)=I_0 \cosh^{-2}(2.634t/t_p)\ , \tag{3.1}$$

where I_0 is the incident intensity which we choose to match the total number of injected carriers, and t_p is the half-width of the pulse. Extra particles are added to the simulation during each time step according to (3.1). To account for spectral broadening of the pulse, the carriers are introduced according to a Gaussian distribution 20 meV wide around the injection energy. Hot phonons are also included here due to their dominant effect in the energy relaxation.[7]

In Fig. 7(a) we show the result for a 500-fs pulse and a relatively small injection density of 5×10^{10} cm^{-2} at different times starting at the end of the laser pulse (the peak of the pulse occurs at 0.7 ps). Here we assume a well width of 150 Å and a small background density of 1×10^{9} cm^{-2} at 5 K. Carriers are injected 150 meV above the bottom of the band. We plot the total occupancy as a function of energy for all the subbands, which is the distribution function times the density of states. As shown, a cascade in the distribution is quite evident and persists up to 1.6 ps due to the relative inefficiency of the *e-e* scattering at this low free-carrier density. The kink in the curve at about 40 meV is the second subband energy.

In Fig. 7(b) we show the relative rates of *e-e* and electron-phonon scattering, calculated from the number of scattering events divided by the total number of particles over each time step. Phonon emission is the dominant scattering mechanism until the distribution has cooled sufficiently (1.6 ps) that *e-e* scattering is more important. Phonon absorption becomes increasingly important due to buildup of nonequilibrium phonons. As shown in Fig. 7(b), the rates of emission and absorption approach one another, resulting in a reduction of the net energy-loss rate.

At an injection density of 5×10^{11} cm^{-2} shown in Fig. 8(a), *e-e* scattering is more effective than the phonon emission, and the features of the cascade are washed out almost resulting in a thermalized (Maxwellian) type of distribution immediately after the pulse is over. The rate of *e-e* scattering is now greater due to the increased density of the injected carriers as shown in Fig. 8(b). Here *e-e* scattering exceeds the phonon emission rate after only 0.5 ps. Phonon absorption due to nonequilibrium phonons becomes important at shorter times due to the higher injected carrier density which generates a greater number of hot phonons.

In the simplified model for screening used here, the screening constant does not depend directly on density which is characteristic of low-temperature screening in a purely two-dimensional system. Thus, the scattering

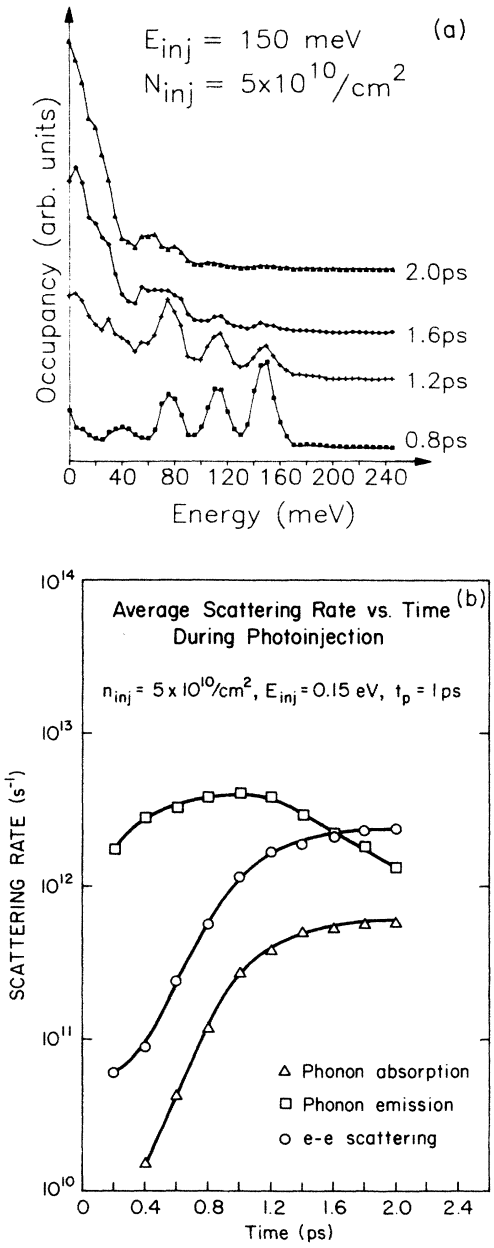

FIG. 7. (a) Electron occupancy as a function of energy for various times after laser excitation and an injection density of 5×10^{10} cm^{-2} at an energy 0.15-eV above the conduction-band edge. (b) Average total scattering rate per electron as a function of time for POP emission (□), absorption (△), and electron-electron (○) scattering.

rate (2.21) is directly proportional to the electron density resulting in the transition from cascadelike to thermalized behavior in the 1×10^{11} cm^{-2} range of carrier densities. If a more complete model for the screening is used, this simple picture will no longer hold as the screening constant depends on density, particularly at high temperatures. At high temperatures, q_0 is directly proportional to density for a 2D system,[27] and therefore *e-e* scattering may be important at lower densities as well. However, the effect of reducing q_0 is to increase small-angle scattering which is ineffective in exchanging energy between particles,[24] and thus the density dependence may be qualitatively the same as we have presented here. The effect of temperature-dependent screening on carrier relaxation in 2D systems is discussed elsewhere.[28]

Due to the intersubband energy exchange arising from *e-e* scattering, redistribution of the carrier kinetic energy occurs and the subband energies tend to equilibrate. This effect is evidenced in Fig. 9 where we plot the carrier temperature (the average kinetic energy) in the lowest and first excited subband as a function of time during laser excitation. In this simulation, we start with a background density of 2.5×10 cm^{-2} carriers at 5 K in the lowest subband and then inject carriers at an energy of 0.25 eV above the lowest subband energy as discussed above. We inject a total of 5×10^{11} cm^{-2} carriers into the band using a 0.6-ps pulse which is centered at $t=1$ ps in Fig. 9. The injected carriers interact with the cold electrons through *e-e* scattering, transferring energy to them and losing energy in the process. As seen in Fig. 9, the electrons in both subbands rapidly reach the same average energy primarily through *e-e* scattering. As shown by the dotted curve of Fig. 9, when *e-e* scattering is absent, the electron temperatures remain quite different after the pulse is over. In Fig. 10, we plot the fractional occupancy of the lowest subband as a function of time with and without *e-e* scattering which shows little difference due to the relative weakness of intersubband *e-e* scattering in the present formalism.

The fraction of carriers which transfer to the L valley does depend on *e-e* scattering, especially at injection energies close to the L-valley energy. This is also shown in Fig. 10 on the left-hand side. More carriers reside in the upper valley at times after the pulse due to spreading of the injected distribution to higher energies before relax-

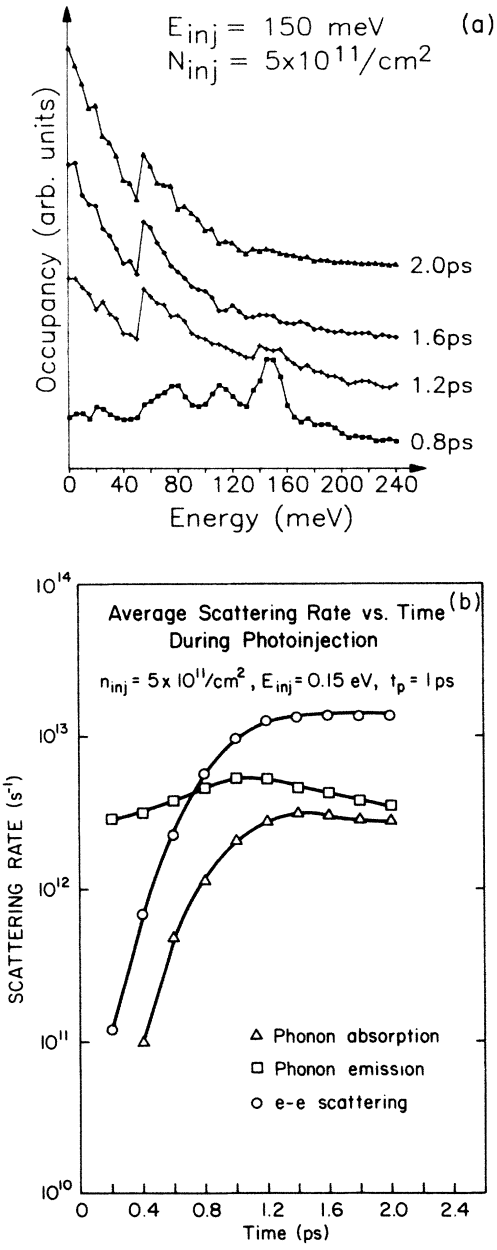

FIG. 8. Electron occupancy as a function of energy for various times after laser excitation and an injection density of 5×10^{11} cm^{-2} at an energy of 0.15 eV above the conduction-band edge. (b) Average total scattering rate per electron as a function of time for POP emission (□), absorption (△), and electron-electron (○) scattering.

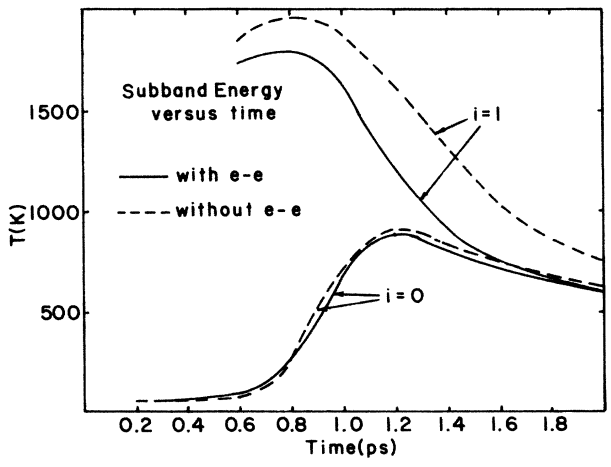

FIG. 9. Average kinetic energy with (solid line) and without (dashed line) *e-e* interaction in the ground ($i=0$) and first-excited ($i=1$) subbands during a 0.6-ps laser pulse which peaks at 1 ps. A background density of 2.5×10^{11} cm^{-2} is assumed with 5×10^{11} cm^{-2} carriers injected at an energy of 0.25 eV.

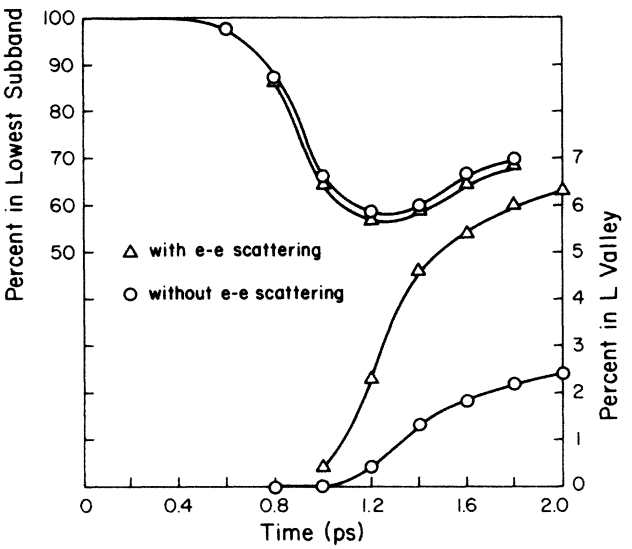

FIG. 10. Occupancy of the ground subband (top curves) with (△) and without (○) *e-e* scattering as a function of time for the same parameters as Fig. 9. Also shown is the occupancy of the *L* valley (bottom curves) with (△) and without (○) *e-e* scattering.

ing, allowing more carriers to transfer than in the case where this mechanism is absent. This fact accounts for the overall lower energy in Fig. 9 of electrons cooling subject to *e-e* scattering. The energy is eventually fed back into the electron system at longer times due to retransfer back from the *L* valley.

IV. CONCLUSIONS AND FUTURE WORK

We have presented a model for *e-e* scattering in a QW system using an ensemble Monte Carlo simulation. This model is capable of describing the carrier dynamics at low temperature through the inclusion of degeneracy and *e-e* scattering, which allows the equilibrium distribution at low temperature to achieve a Fermi-Dirac distribution in the simulation. With an applied electric field, *e-e* scattering is found to be effective in the 2D QW system in removing the kink in the distribution associated with phonon emission. Comparison of the calculated steady-state distribution function for various applied electric fields with photoluminescence results[33] show agreement in the gross features, but give consistently smaller electron temperatures as derived from the high-energy tail of the distribution.

We show that the shape of the distribution function is controlled by *e-e* scattering during and after laser excitation. For low carrier densities, *e-e* scattering is weak and electrons relax their energy via a cascade of successive optical-phonon emissions. For higher carrier densities, *e-e* scattering is more effective in setting up a heated Maxwellian distribution which absorbs the energy of the injected electrons before they can emit an optical phonon, thus suppressing the cascade. Our results show that thermalization of the carrier energy between subbands occurs quite rapidly through *e-e* scattering shortly after the end of the laser pulse. The exact scattering rate due to *e-e* scattering depends strongly on screening which is formally difficult in the multisubband system. We have used a low-temperature screening constant for the present work which overestimates the screening, and thus *e-e* scattering may be important at low electron densities as well. In future investigations, we will include heating effects on the 2D screening which our preliminary results show enhances the rate of *e-e* scattering during laser excitation.

ACKNOWLEDGMENTS

The authors would like to express their gratitude to R. Brunetti, C. Jacoboni, P. Kocevar, and J. Shah for many useful discussions related to this work. We would also like to acknowledge financial support from the Alexander von Humboldt Foundation in this research.

[1]J. L. Oudar, D. Hulin, A. Migus, and A. Antonetti, Phys. Rev. Lett. **55**, 2074 (1985).
[2]W. H. Knox, C. Hirlimann, D. A. B. Miller, J. Shah, D. S. Chemla, and C. V. Shank, Phys. Rev. Lett. **56**, 1191 (1986).
[3]J. F. Ryan, R. A. Taylor, A. J. Turberfield, A. Maciel, J. M. Worlock, A. C. Gossard, and W. Wiegmann, Phys. Rev. Lett. **53**, 1841 (1984).
[4]J. Shah, A. Pinczuk, A. C. Gossard, and W. Wiegmann, Phys. Rev. Lett. **54**, 2045 (1985).
[5]C. H. Yang, J. M. Carlson-Swindle, S. A. Lyon, and J. M. Worlock, Phys. Rev. Lett. **55**, 2359 (1985).
[6]D. N. Mirlin, I. Ya Karlik, L. P. Nikitin, I. I. Reshina, and V. F. Sapega, Solid State Commun. **37**, 757 (1980).
[7]S. M. Goodnick and P. Lugli, in *Proceedings of the 18th International Conference on the Physics of Semiconductors*, edited by O. Engström (World-Scientific, Singapore, 1987), pp. 1334–1338.
[8]S. M. Goodnick and P. Lugli, in *High-Speed Electronics*, edited by B. Kallack and H. Beneking (Springer-Verlag, Berlin, 1986).
[9]M. Tomizawa, K. Yokoyama, and A. Yoshii, IEEE Electron Dev. Lett. **EDL-5**, 464 (1984).
[10]K. Yokoyama and K. Hess, Phys. Rev. B **33**, 5595 (1986).
[11]M. Al-Mudares and B. K. Ridley, Physica **134B**, 526 (1985).
[12]P. Lugli, S. M. Goodnick, and F. Koch, Superlatt. Microstruct. **2**, 335 (1986).
[13]T. Ando, A. B. Fowler, and F. Stern, Rev. Mod. Phys. **54**, 437 (1982).
[14]P. J. Price, Ann. Phys. (N.Y.) **133**, 217 (1981).
[15]F. A. Riddoch and B. K. Ridley, J. Phys. C **16**, 6971 (1983).
[16]F. A. Riddoch and B. K. Ridley, Physica **134B**, 342 (1985).
[17]C. H. Yang and S. A. Lyon, Physica **134B**, 309 (1985).
[18]S. Das Sarma, W. Y. Lai, and A. Kobayashi, in *Proceedings of the 18th International Conference on the Physics of Semi-*

conductors, Ref. 7, pp. 651–654.
[19]P. J. Price, Phys. Rev. B **30**, 2234 (1984).
[20]D. K. Ferry, Surf. Sci. **57**, 218 (1976).
[21]E. Abrahams, Phys. Rev. **95**, 839 (1954).
[22]J. M. Ziman, *Electrons and Phonons* (Oxford University Press, London, 1960), pp. 170–172.
[23]N. Takenaka, M. Inoue, and Y. Inuishi, J. Phys. Soc. Jpn. **47**, 861 (1979).
[24]C. J. Hearn, in *The Physics of Nonlinear Transport in Semiconductors,* edited by D. K. Ferry, J. R. Barker, and C. Jacoboni (Plenum, New York, 1980), pp. 153–166.
[25]E. D. Siggia and P. C. Kwok, Phys. Rev. B **2**, 1024 (1970).
[26]F. Stern, Phys. Rev. Lett. **18**, 5009 (1978).
[27]A. L. Fetter, Phys. Rev. B **10**, 3739 (1974).
[28]S. M. Goodnick and P. Lugli, Appl. Phys. Lett. **51**, 584 (1987).
[29]C. Jacoboni and L. Reggiani, Rev. Mod. Phys. **65**, 645 (1983).
[30]S. Bosi and C. Jacoboni, J. Phys. C **9**, 315 (1976).
[31]P. Lugli and D. K. Ferry, IEEE Trans. Electron Dev. **ED-32**, 2431 (1985).
[32]R. Brunetti, C. Jacoboni, A. Matulionis, and V. Dienys, Physica **134B**, 369 (1985).
[33]J. Shah, A. Pinczuk, H. L. Störmer, A. C. Gossard, and W. Wiegmann, Appl. Phys. Lett. **44**, 322 (1984).
[34]S. A. Lyon, J. Lumin. **35**, 121 (1986).
[35]P. Kocevar (private communication).

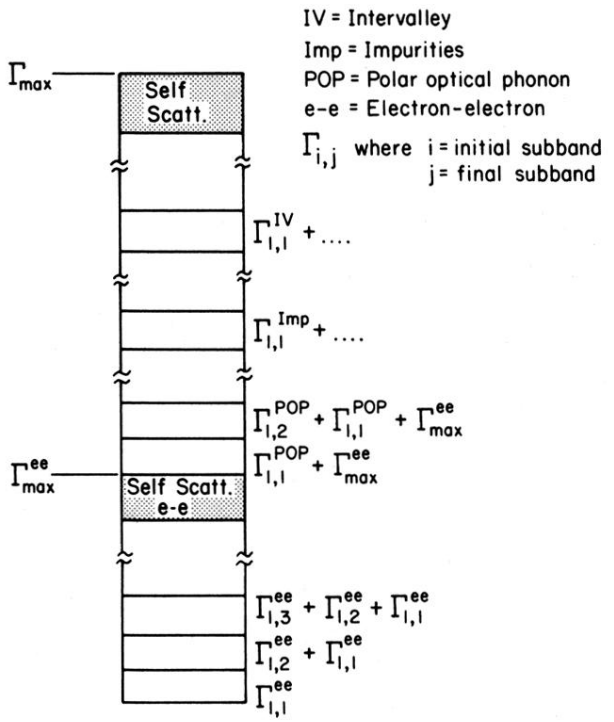

FIG. 3. Histogram of the various scattering rates in the Monte Carlo simulation.